HiSST: 2nd International Conference on
High-Speed Vehicle Science & Technology
11–15 September 2022, Bruges, Belgium

Numerical analysis of the flow in a generic scramjet engine model - Flow without injection

Fábio Henrique Eugênio Ribeiro[1], *André Carlos Fraile Júnior*[2]

Abstract

Scramjet engines are high-speed airbreathing propulsion systems with no moving parts, which compress the air dynamically through a supersonic intake, increasing temperature and pressure levels so combustion can occur. Flow dynamics in a generic scramjet combustion chamber is studied based on a representative experiment run at the Institute for Advanced Studies. The computations are performed with an in-house solver that is being developed to perform simulations of compressible reactive multi-component flows. The present simulations are performed within the LES framework and WALE model is retained as the SGS viscosity closure, and the geometry of the combustor is modeled using the IBM algorithm.

Keywords: *CFD, scramjet, turbulence*

Nomenclature

Latin

D_{inj} – Injection diameter
e – Internal specific energy
e_t – Total specific energy
IQ_η – Celik quality index
$\mathcal{L}_\eta$ – Kolmogorov length scale
$\mathcal{N}_{sp}$ – Number of chemical species
p – Pressure
p_0 – Initial pressure
$\mathcal{R}$ – Gas constant
S_n – Probe n
T – Temperature
T_0 – Initial temperature
t – Time
t_0 – Initial time
t^* – Normalized time
u_i – Velocity component in direction i
u_∞ – Nominal flow velocity
$V_{\alpha,i}$ – Diffusion velocity component in direction i of species α
$\mathcal{W}$ – Mixture molar weight
$\mathcal{W}_\alpha$ – Molar weight of species α
x_j – Cartesian coordinate in direction j
Y_α – Mass fraction of species α

Greek

Δ – Characteristic mesh size
Δx_i – Points concentration parameter at i-axis
$\Delta x_{i,cur}$ – Current mesh size at i-axis
$\Delta x_{i,max}$ – Largest mesh size at i-axis
$\Delta x_{i,min}$ – Smallest mesh size at i-axis
μ – Dynamic viscosity
ρ – Density
$\bar{\tau}_{ij}$ – Filtered stress tensor
$\dot{\omega}_\alpha$ – Chemical rate of species α

1. Introduction

One of the main advantages of scramjet engines over concurrent technologies is that they do not need to carry oxidizer, which is obtained directly from the atmosphere, thus providing weight reduction and allowing higher payloads and specific impulse when compared to standard rocket engines. However, as it does not produce any thrust at zero velocity, it must be ignited after being accelerated by another kind of engine to its takeover speed.

[1]*Institute for Advanced Studies, Trevo Coronel Aviador José Alberto Albano do Amarante, 1 - São José dos Campos - SP - Brazil, henriquefher@fab.mil.br*
[2]*Institute for Advanced Studies, Trevo Coronel Aviador José Alberto Albano do Amarante, 1 - São José dos Campos - SP - Brazil, fraileacfj@fab.mil.br*

Still today there are no scramjet engines being used in practical devices, even tough many achievements have been obtained since the early sixties. The combustion chamber is crossed by a supersonic flow, limiting considerably the time available to inject fuel, mix it with the oxidizer, ignite the resulting mixture and stabilize combustion. One of the most challenging issues seems to be combustion stabilization.

In the present numerical study, such high-speed flow conditions are scrutinized on the basis of numerical simulations of a scramjet engine model representative of experiments that are being conducted at the Institude for Advanced Studies, in Brazil, initially without any kind of injection. The purpose is to validate the CFD code by comparing the pressures measured at the walls of the combustion chamber. The simplified computational geometry consists of a constant section channel, followed by a diverging section.

2. Governing equations and numerical methods

2.1. Compressible Large-Eddy Simulation formulation

The set of filtered Navier-Stokes equations are expressed below, in its conservative form:

$$\frac{\partial \bar{\rho}}{\partial t} + \frac{\partial \bar{\rho}\widetilde{u}_i}{\partial x_i} = 0 \tag{1}$$

$$\frac{\partial \bar{\rho}\widetilde{u}_j}{\partial t} + \frac{\partial \bar{\rho}\widetilde{u}_i\widetilde{u}_j}{\partial x_i} = -\frac{\partial \bar{p}}{\partial x_j} + \frac{\partial \bar{\tau}_{ij}}{\partial x_i} - \frac{\partial}{\partial x_i}\left(\overline{\rho u_i u_j} - \bar{\rho}\widetilde{u}_i\widetilde{u}_j\right) \tag{2}$$

$$\frac{\partial \bar{\rho}\widetilde{e}_t}{\partial t} + \frac{\partial \bar{\rho}\widetilde{u}_i\widetilde{e}_t}{\partial x_i} = -\frac{\partial \bar{p}\widetilde{u}_i}{\partial x_i} + \frac{\partial \widetilde{u}_i\bar{\tau}_{ij}}{\partial x_j} - \frac{\partial \bar{\mathcal{J}}_i}{\partial x_i} - \frac{\partial}{\partial x_i}\left(\overline{\left(\rho e_t + p\right)u_i} - \left(\bar{\rho}\widetilde{e}_t + \bar{p}\right)\widetilde{u}_i\right) \tag{3}$$

$$\frac{\partial \bar{\rho}\widetilde{Y}_\alpha}{\partial t} + \frac{\partial \bar{\rho}\widetilde{u}_i\widetilde{Y}_\alpha}{\partial x_i} = -\frac{\partial \overline{\rho Y_\alpha V_{\alpha,i}}}{\partial x_i} + \bar{\rho}\widetilde{\dot{\omega}}_\alpha - \frac{\partial}{x_i}\left(\overline{\rho Y_\alpha u_i} - \bar{\rho}\widetilde{Y}_\alpha\widetilde{u}_i\right) \tag{4}$$

with t being time, x_j the Cartesian coordinate in direction j ($j = 1, ..., 3$), u_i the velocity component in direction i ($i = 1, ..., 3$), ρ the density, p the pressure, $e_t = e + u_i u_i/2$ the total specific energy (the sum of the internal specific energy, e, and the kinetic energy), and Y_α the mass fraction of species α ($\alpha = 1, ..., \mathcal{N}_{sp}$). The integer $\mathcal{N}_{sp}$ denotes the number of chemical species. The thermodynamic variables are interrelated through the filtered pressure field approximated from $\bar{p} = \bar{\rho}\mathcal{R}\widetilde{T}/\mathcal{W}$, with $\mathcal{R}$ being the gas constant, T the temperature and $\mathcal{W}^{-1} = \sum_{\alpha=1}^{\mathcal{N}_{sp}} \widetilde{Y}_\alpha/\mathcal{W}_\alpha$ the molar weight of the mixture.

The diffusion velocity and the chemical production rate of species α are denoted, respectively, by $V_{\alpha,i}$ and $\dot{\omega}_\alpha$. Filtered tensors are calculated from $\bar{\tau}_{ij} = 2\widetilde{\mu}\left(\widetilde{S}_{ij} - \widetilde{S}_{kk}\delta_{ij}/3\right)$, with $\widetilde{S}_{ij} = \left(\partial\widetilde{u}_i/\partial x_j + \partial\widetilde{u}_i/\partial x_j\right)/2$. The filtered equations are the same used by Ragab *et al.*[1], Piomelli *et al.*[2], Kosović *et al.*[3] and Dubois *et al.*[4].

Molecular diffusion terms are calculated from the species mixture formulation [5] and the filtered diffusion molecular and heat fluxes are deduced from their instantaneous expressions, but applied to its filtered quantities. The diffusion molecular flux from species α can then be approximated by:

$$\overline{\rho Y_\alpha V_{\alpha,i}} = -\bar{\rho}\widetilde{D}^m_\alpha \frac{\mathcal{W}_\alpha}{\widetilde{\mathcal{W}}}\frac{\partial \widetilde{X}_\alpha}{\partial x_i} + \bar{\rho}\widetilde{Y}_\alpha\widetilde{V}^c_i \tag{5}$$

where X_α is the molar fraction of species α and $\widetilde{D}^m_\alpha$ is the matrix of the diffusion flux coefficients from the same species. The last term of Eq. 5 is a correction term that is used to ensure mass conservation.

The i-component of the filtered head flux is calculated from equation below:

$$\overline{\mathcal{J}}_i = -\widetilde{\lambda}\frac{\partial \widetilde{T}}{\partial x_i} + \sum_{\alpha=1}^{\mathcal{N}_{sp}} \bar{\rho}\widetilde{Y}_\alpha \widetilde{V}_{\alpha,i}\widetilde{h}_\alpha \tag{6}$$

where $\widetilde{\lambda}$ is the mixture thermal conductivity, calculated from the filtered values.

The subgrid (SGS) tensor $T_{ij} = \overline{\rho u_i u_j} - \bar{\rho}\widetilde{u}_i\widetilde{u}_j$ is modeled with Boussinesq framework.

Finally, the last term of the filtered energy equation, i.e. Eq. 3, is calculated as below:

$$\overline{(\rho e_t + p)\, u_j} - (\bar{\rho}\widetilde{e}_t + \bar{p})\,\widetilde{u}_j = \underbrace{\left[\overline{\rho c_p T u_j} - \bar{\rho}\bar{c}_p\widetilde{T}\widetilde{u}_j\right]}_{\mathcal{Q}_j} + \underbrace{\left[\frac{1}{2}\left(\overline{\rho u_i u_i u_j} - \bar{\rho}\widetilde{u}_i\widetilde{u}_i\widetilde{u}_j\right)\right]}_{\psi_{iij}} - \frac{1}{2}T_{ii}\widetilde{u}_j \tag{7}$$

where $\mathcal{Q}_j = -\lambda_{sgs}\partial\widetilde{T}/\partial x_j$ is the subgrid heat flux modeled from the approximation of the diffusion gradient, with $\lambda_{sgs} = \mu_{sgs}\bar{c}_p/\mathrm{Pr}_{sgs}$ being the subgrid thermal conductivity and Pr_{sgs} the subgrid Prandtl number. Quantity ψ_{iij} characterizes the velocity correlation tensor, obtained from Daly & Harlow[6] expression: $\psi_{ijk} = C_{c_3}\nu_{sgs}\partial T_{ij}/\partial x_k$.

Subgrid viscosity μ_{sgs} is calculated from Nicoud & Ducros[7] WALE (Wall-Adapting Local Eddy) model:

$$\mu_{sgs} = \bar{\rho}\left(C_w\Delta\right)^2 \frac{\left(S^d_{ij}S^d_{ij}\right)^{3/2}}{\left(\widetilde{S}_{ij}\widetilde{S}_{ij}\right)^{5/2} + \left(S^d_{ij}S^d_{ij}\right)^{5/4}} \tag{8}$$

where $C_w = C_s\sqrt{10.6}$ is the WALE model constant, $\Delta = \left(\Delta x_1 \Delta x_2 \Delta x_3\right)^{1/3}$ is the characteristic mesh size and

$$S^d_{ij} = \frac{1}{2}\left(\frac{\partial\widetilde{u}_i}{\partial x_l}\frac{\partial\widetilde{u}_l}{\partial x_j} + \frac{\partial\widetilde{u}_j}{\partial x_l}\frac{\partial\widetilde{u}_l}{\partial x_i}\right) - \frac{1}{3}\frac{\partial\widetilde{u}_m}{\partial x_l}\frac{\partial\widetilde{u}_l}{\partial x_m}\delta_{ij} \tag{9}$$

Other closing parameters are the same previously considered by Techer *et al.*[8]. The filtered formation rate of species $\widetilde{\dot{\omega}}_\alpha$, when applicable, are calculated considered the PSR (Perfectly Stirred Reactor) reactor model and the O'Conaire *et al.*[9] reaction mechanism, which has 9 species (H_2, O_2, H_2O, H, O, OH, HO_2, H_2O_2 and N_2) and 21 elementary steps that represents H_2-air chemistry.

2.2. Numerical methods

The solver used in the simulations performs the temporal integration with an explicit third-order total-variation-diminishing (TVD) scheme and uses the optimal seventh-order accurate flux reconstruction and the application of the non-linear upwinding procedure conditioned to a smoothness criterion that involves the local values of the normalized spatial variations of both pressure and density. Viscous and molecular diffusion fluxes are computed with an eighth-order centered difference scheme.

3. Computational setup

The experimental geometry corresponds to the T1 shock tunnel facility located on the Institute for Advanced Studies, which consists of a supersonic nozzle that accelerates the flow to the desired condition. Fig. 1 presents the experimental scheme, with the simulation region in gray.

Figure 2 presents the central plane ($x_3/D_{inj} = 0$) of the computational domain with an isolator with $l_1/D_{inj} = 25.5075$ and a ramp with $l_2/D_{inj} = 75.005$ and inclination of $\alpha = 4.00°$, followed by another section with $l_3/D_{inj} = 6.9875$. Although there is an injection orifice with diameter D_{inj}, which is used in experiments with injection, for the sake of simplicity, it is not modeled in the computation domain as the current experiment does not have any kind of injection in the flow. This injection orifice is located at $x_{inj}/D_{inj} = 5.6175$ before the ramp, along its axis, at the central plane $x_3/D_{inj} = 0$. The distance between the lower and the upper walls is $h_1/D_{inj} = 5$ and the domain is $x_3/D_{inj} = 7$ wide, symmetrical

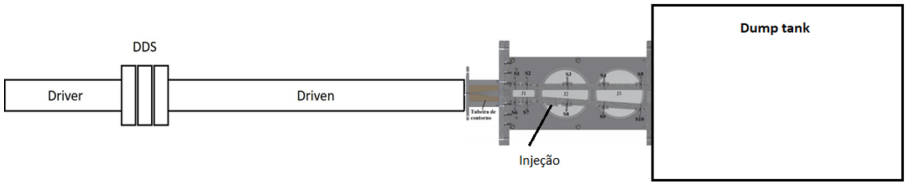

Fig 1. Experimental scheme

to the central plane. The origin $\mathcal{O}$ of the computational domain is located at the beginning of the lower wall of the isolator, along the central plane $x_3/D_{inj} = 0$.

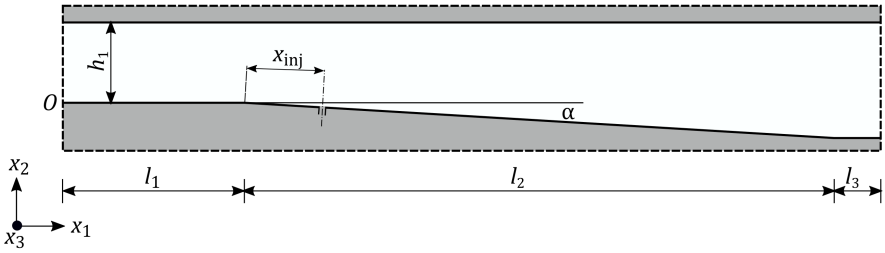

Fig 2. Experimental scheme

Several probes are placed at the computational domain, at the same locations of the pressure sensors, presented in table 1 and illustrated in Fig. 3.

Table 1. Probes location

Probe	x_1/D_{inj}	x_2/D_{inj}	x_3/D_{inj}
S_1	$+96.025$	$+5.000$	$+0.000$
S_2	$+69.215$	$+5.000$	$+0.000$
S_3	$+42.405$	$+5.000$	$+0.000$
S_4	$+12.750$	$+5.000$	$+0.000$
S_5	$+4.000$	$+5.000$	$+0.000$
S_6	$+96.025$	-4.930	$+0.000$
S_7	$+69.215$	-3.055	$+0.000$
S_8	$+42.405$	-1.180	$+0.000$
S_9	$+12.750$	$+0.000$	$+0.000$
S_{10}	$+4.000$	$+0.000$	$+0.000$

Time is normalized as $t^* = (t \cdot u_\infty)/D_{inj}$, with u_∞ being the nominal flow velocity. Simulation begins at $t_0 = t^* = 0.0$ with the flow at rest with $T_0 = 298.0$ K, $p_0 = 0.96$ kPa and $(Y_{O_2,Y_{N_2}}) = (0.21, 0.79)$, and runs until $t^* = 1800.0$, with data being saved at 2.0 MHz from t_0.

The 3D computational domain consists in a Cartesian mesh of approximately $36\ 000\ 000$ points ($\overline{\Delta x_1} \approx 505.5\ \mu$m, $\overline{\Delta x_2} \approx 164.1\ \mu$m, $\overline{\Delta x_3} \approx 160.3\ \mu$m). Upper and lower walls are modeled using the `IBM` (Immersed Boundary Method [10]) framework. All walls are adiabatic.

A normalized parameter of points concentration Δx_i was used, shown in Eq. 10, going from 0.0 (lower concentration of points: larger characteristic mesh size) up to 1.0 (higher concentration of points: smaller characteristic mesh size).

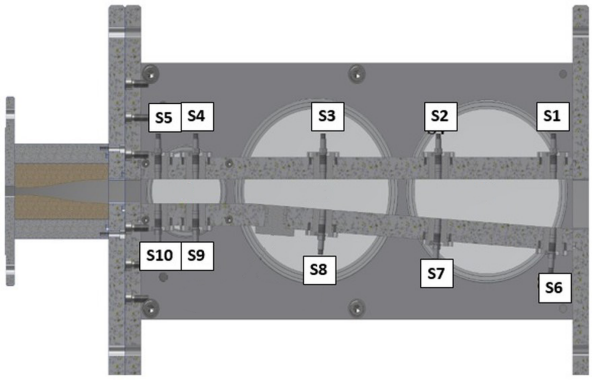

Fig 3. Probes location

$$\Delta x_i = 1 + \frac{\Delta x_{i,min} - \Delta x_{i,cur}}{\Delta x_{i,max} - \Delta x_{i,min}} \tag{10}$$

where Δx_i is the points concentration parameter, $\Delta x_{i,min}$ is the smallest mesh size, $\Delta x_{i,max}$ is the largest mesh size, and $\Delta x_{i,cur}$ is the current mesh size. These parameters of points concentration are presented in Fig. 4:

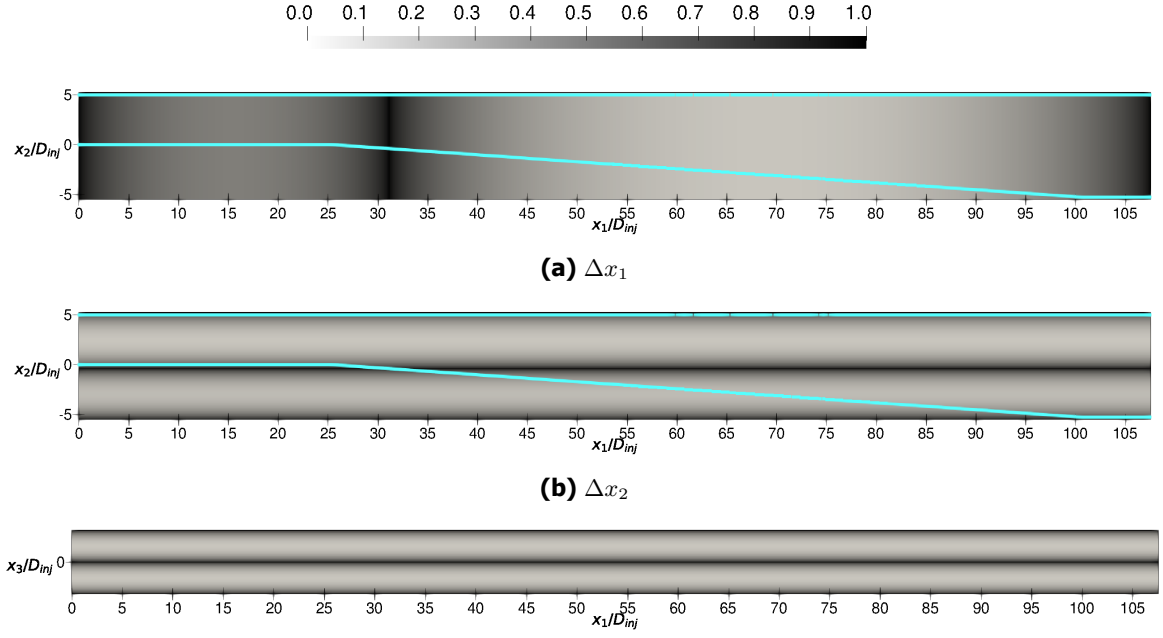

(a) Δx_1

(b) Δx_2

(c) Δx_3

Fig 4. Normalized parameter of points concentration obtained at $x_3/D_{inj} = 0$ (IBM walls in cyan)

3.1. Mesh verification

Celik index [11] was the choice to verify the mesh quality as it is less sensible to the mesh modeling, being based on the characteristic mesh size Δ and the Kolmogorov length scale $\mathcal{L}_\eta$, and defined as:

$$IQ_\eta = \left[1 + \alpha_\eta \left(\frac{\Delta}{\mathcal{L}_\eta}\right)^m\right]^{-1} \tag{11}$$

with $(\alpha_\eta, m) = (0.05, 0.5)$, $\mathcal{L}_\eta = \left(\nu^3/\varepsilon\right)^{1/4}$ and ε being the turbulent kinetic energy dissipation rate. About this index, it is important to mention that, in a DNS simulation, $k_{max}\mathcal{L}_\eta = 3/2$ so as, with k_{max} being at the order of π/Δ, then $\Delta/\mathcal{L}_\eta \approx 2.0$, which results in $IQ_\eta = 0.93$. It means that, when $IQ_\eta \geq 0.93$, the mesh, has a resolution level equivalent to a DNS simulation.

Fig. 5 presents the Celik quality index in the computational domain in the central plane ($x_3/D_{inj} = 0$), where one can check that most part of the mesh presents optimal resolution:

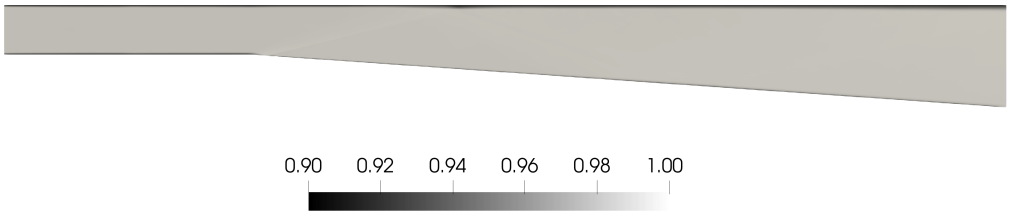

Fig 5. Celik quality index

From the Probability Distribution Function (PDF) of this index, it can be verified that most of the points presents resolution that indicates a well resolved mesh, as presented in Fig. 6:

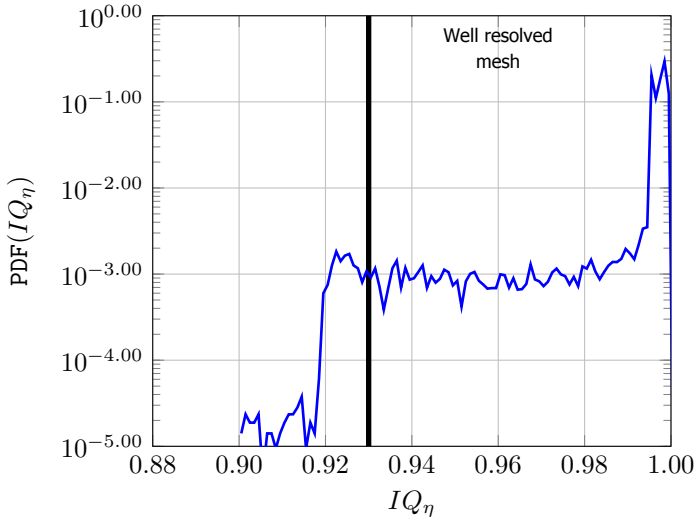

Fig 6. Probability Distribution Function of the Celik quality index

A Cumulative Distribution Function (CDF) can be expressed from a PDF (Probability Distribution Function) by:

$$\mathbb{F}(x) = \int_0^x \mathrm{PDF}\left(IQ_\eta\right) \mathrm{d}IQ \tag{12}$$

and its complement by:

$$1 - \mathbb{F}(x) = 1 - \int_0^x \mathrm{PDF}\left(IQ_\eta\right) \mathrm{d}IQ \tag{13}$$

The result of Eq. 13 represents the probability of IQ_η being larger than a specific value. Fig. 7 indicates that approximately 98% of the points in the mesh has $IQ_\eta > 0.93$, which means that the mesh presents an optimal resolution.

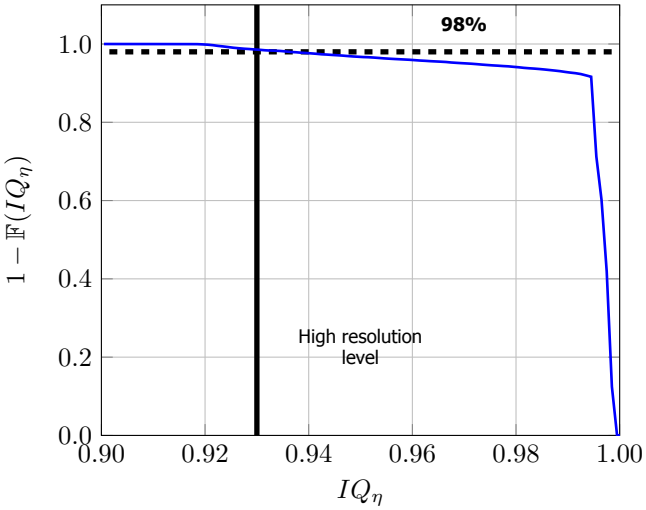

Fig 7. Cumulative Distribution Function of the Celik quality index

Furthermore, as the probes are located near the walls of the computational domain, the mesh solution must be verified in order to correctly capture the resolved scales. Table 2 presents the recommended magnitude orders for a Wall Resolved LES.

Table 2. Recommended magnitude order for a Wall Resolved LES

	DNS	LES
Δx^+	$10 - 15$	$50 - 150$
Δy^+	1	< 2

Fig. 8 presents the mesh size distribution in wall units along all the IBM region, as performed by Techer[12], where one can notice that the mesh presents optimal resolution, specially along x-axis.

Moreover, the normalized average velocity u^+ at the probes location were checked, as presented in Fig. 9, plotted in wall units, where these profiles confirm that the WALE model satisfactorily changes its behavior in the buffer layer that separates the logarithmic zone ($y^+ > 30.0$) from the viscous sublayer ($y^+ < 5.0$)[7].

Then we proceed with a statistical convergence analysis so as to verify the convergence of the second-order moment, calculated according to Eq. 14:

$$\sigma\left(u_i u_i\right) = \langle \bar{u}_i \bar{u}_i \rangle - \langle \bar{u}_i \rangle \langle \bar{u}_i \rangle - \left(\bar{u}_i - \langle \bar{u}_i \rangle\right)^2 \tag{14}$$

Fig. 10 presents the statistical convergence for velocities u_x and v_y at the probes coordinates, where one can notice that the solution converges from $t^* \approx 1000$. Therefore, the statistical postprocessing of the computational results will take into account the snapshots obtained from this time up to the end of the simulation.

4. Simulation results

The pressures obtained from the sensors and the values calculated at the probes are presented in Fig. 11. One can verify that sensors S_4 and S_8 had some problems on their measurements as the

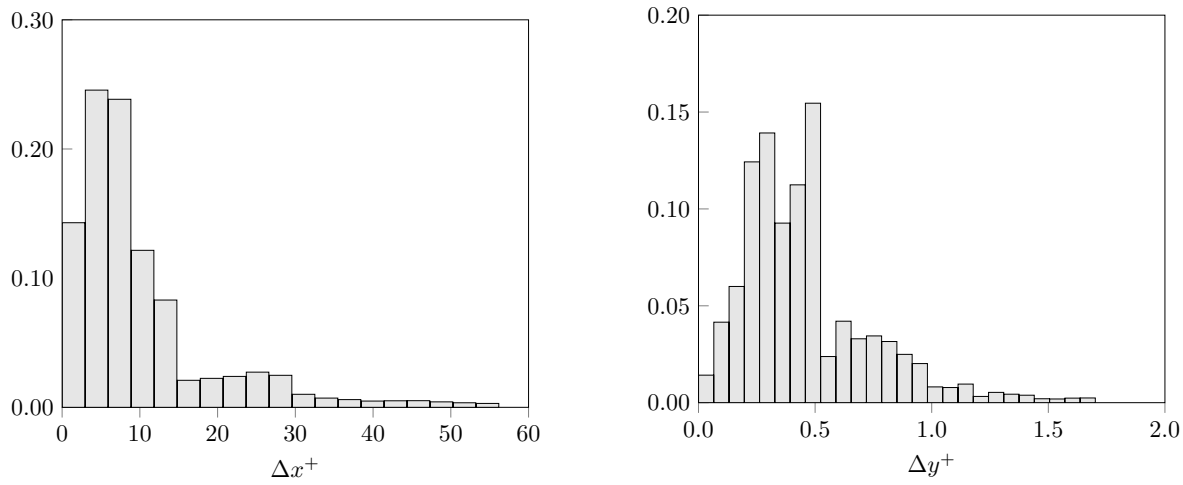

(a) x-axis **(b)** y-axis

Fig 8. Mesh size distribution histogram

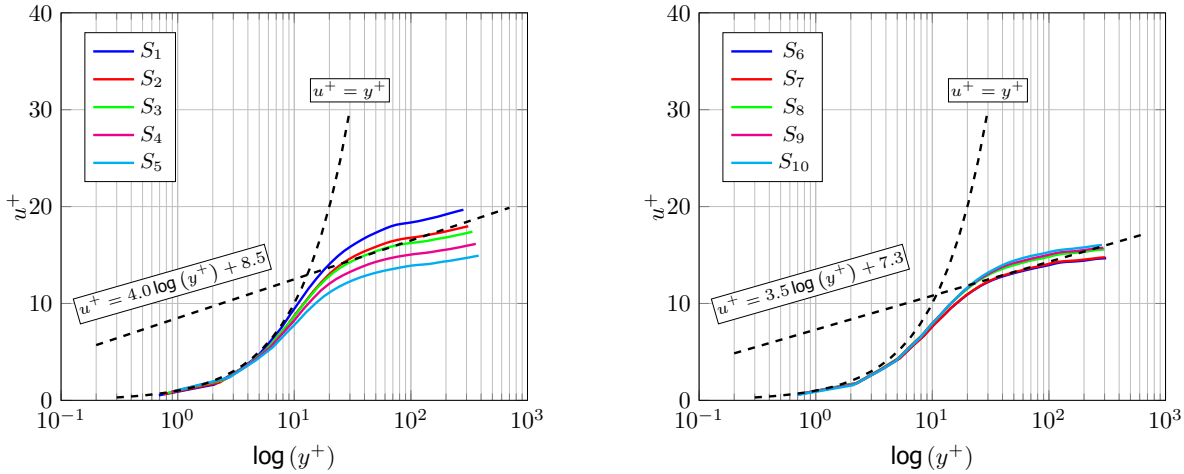

(a) Top wall **(b)** Bottom wall

Fig 9. Non dimensional velocity profile in wall units at several locations x_1/D_{inj} along $x_3/D_{inj} = 0$

pressure increases and then decreases to values near the initial ones.

As the experiment was performed in a shock tunnel (flow flow is not steady) and the simulation was run considering steady flow, the gray part of the graph (between $t^* \approx 1050.0$ and $t^* \approx 1400.0$) is the region where the flow was considered stable, being, then the region considered for the analysis.

Fig. 12 presents the errors between the measured values (from the sensors) and the calculated ones (from the probes). Except for probes S_4 and S_8, all the errors were kept below 20% in the considered time range. Although relatively high, this error is acceptable as the experiment were performed in a shock tunnel, which does not allow the measurements from the sensor to stabilize.

Mach number, temperature and pressure fields, normalized by the initial conditions, are shown in figures 13, 14 and 15, respectively, where one can notice, specially in the pressure field, soft oscillations at the beginning of the computational domain, which corresponds to the coupling of the combustion chamber

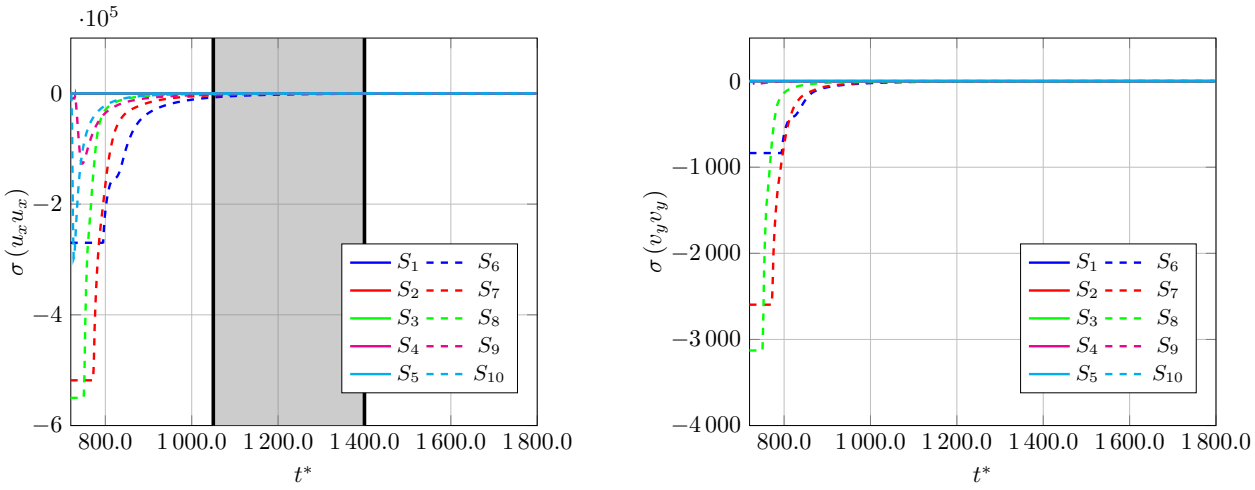

(a) u_x **(b)** v_y

Fig 10. Statistical convergence of the second-order moment

to the experimental facility, as well as oscillations after the ramp, and the reflections at the bottom and at the top wall.

Finally, Fig. 16 presents a Schlieren photo from the experiment and its numerical correspondent, where it can be noticed the presence of a pressure discontinuity at the beginning of the ramp and its reflection at the top wall, near probes S_3 and S_8.

5. Next steps

Once the solver is validated with this kind of flow, without injection, the computational setup will be configured to add injection of a non-reactive gas and reactive gas (hydrogen) to compare with experimental data, as well as analyze the combustion development and the behavior of this representative scramjet combustion chamber.

6. Conclusion

This paper presents the numerical analysis of an experiment run at the Institute for Advanced Studies with a supersonic flow inside a combustion chamber, without any kind of fuel injection, in order to validate the CFD solver.

The numerical simulation made use of LES and IBM framework, considering the same conditions of the experiment.

Due to the computational power and the required time for pre and post-processing, the simulation was run in 2D. Although LES has no meaning when run in 2D because of vorticity effects, this framework was considered despite DNS because of a lighter mesh. An extensive analysis of the mesh quality was performed to ensure its optimal resolution and the capture of the large and small scales.

When comparing the results obtained by the sensors in the experiment with their correspondent numerical probes, all of them presented errors below 20%, except for sensors S_4 and S_8, which failed during the experiment. As the simulation was run in 2D considering a continuous flow, these errors are acceptable, despite the experiment was run in a shock tunnel.

Moreover, Mach, temperature and pressure fields were presented, as well as a comparison between the experiment and the numerical Schlieren, which presented good results.

As next steps, a simulation with non rective gas injection and with fuel injection may be run in order to compare the results with their correspondent experiments.

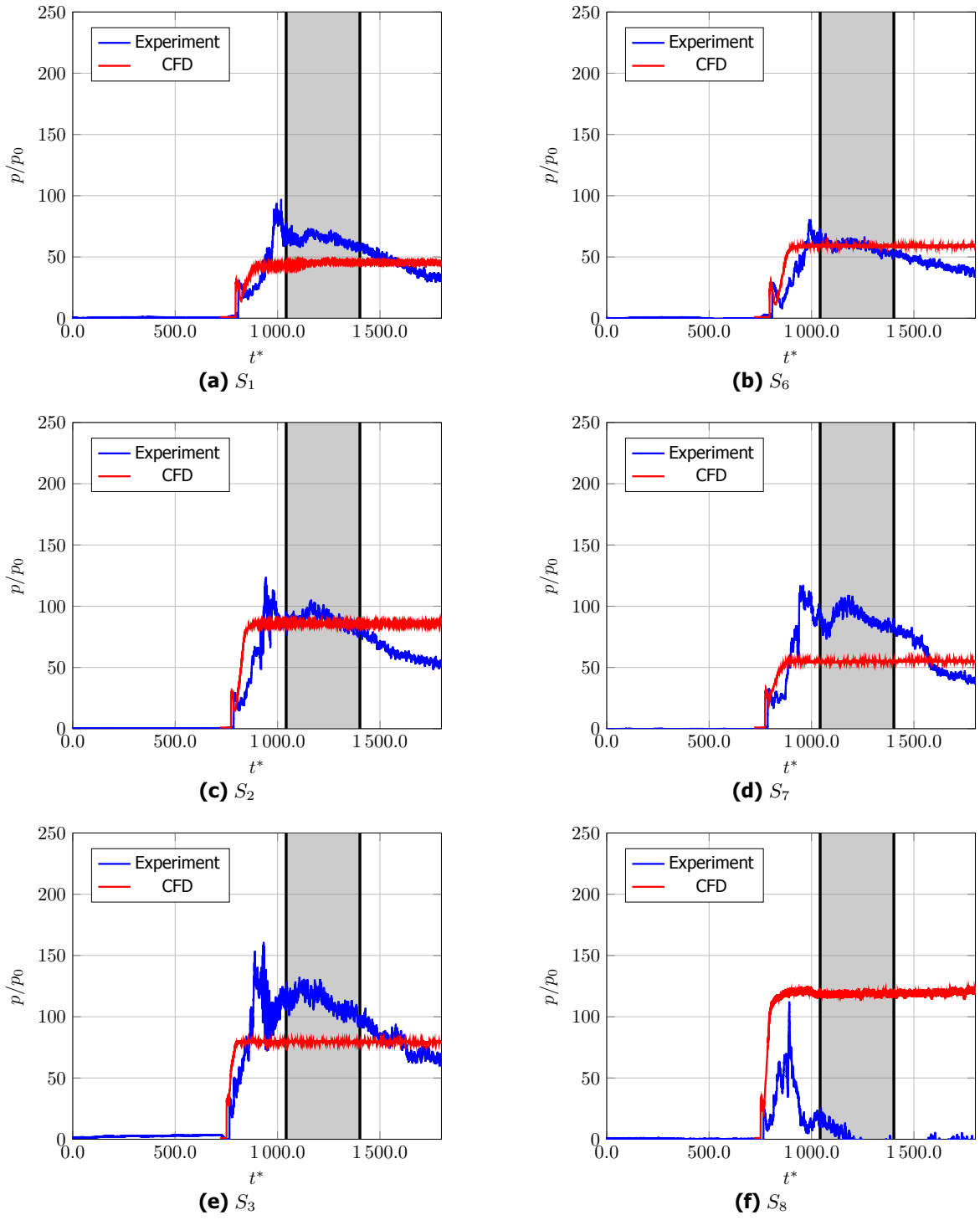

(a) S_1 **(b)** S_6 **(c)** S_2 **(d)** S_7 **(e)** S_3 **(f)** S_8

Fig 11. Pressures measured in the experiment and calculated in the simulation

References

1. Ragab, S., Sheen, S.-C. & Sreedhar, M. *An investigation of finite-difference methods for large-eddy simulation of a mixing layer* in *30th Aerospace Sciences Meeting and Exhibit* AIAA Paper 1992–554 (1992).

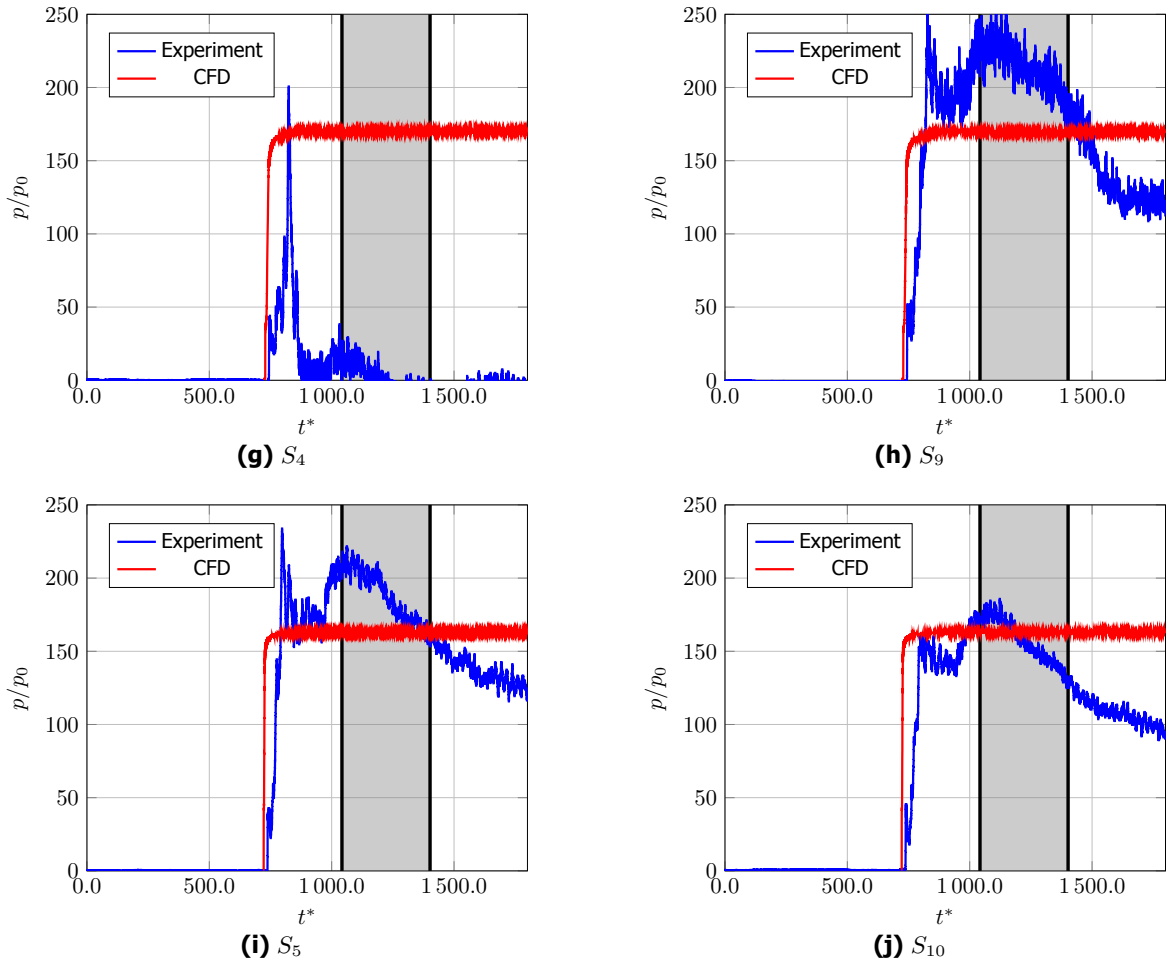

(g) S_4 **(h)** S_9

(i) S_5 **(j)** S_{10}

Fig 11. Pressures measured in the experiment and calculated in the simulation (cont.)

2. Piomelli, U. & Chasnov, J. R. in *Turbulence and Transition Modelling* 269–336 (Springer, 1996).
3. Kosović, B., Pullin, D. I. & Samtaney, R. Subgrid-scale modeling for large-eddy simulations of compressible turbulence. *Physics of Fluids* **14,** 1511–1522 (2002).
4. Dubois, T., Domaradzki, J. & Honein, A. The subgrid-scale estimation model applied to large eddy simulations of compressible turbulence. *Physics of Fluids* **14,** 1781–1801 (2002).
5. Hirschfelder, J. & Curtiss, C. The theory of flame propagation. *The Journal of Chemical Physics* **17,** 1076–1081 (1949).
6. Daly, B. & Harlow, F. Transport equations in turbulence. *The Physics of Fluids* **13,** 2634–2649 (1970).
7. Nicoud, F. & Ducros, F. Subgrid-scale stress modelling based on the square of the velocity gradient tensor. *Flow, Turbulence and Combustion* **62,** 183–200 (1999).
8. Techer, A., Moule, Y., Lehnasch, G. & Mura, A. Mixing of Fuel Jet in Supersonic Crossflow: Estimation of Subgrid-Scale Scalar Fluctuations. *AIAA Journal,* 465–481 (2018).
9. O'Conaire, M., Curran, H. J., Simmie, J. M., Pitz, W. J. & Westbrook, C. K. A comprehensive modeling study of hydrogen oxidation. *International Journal of Chemical Kinetics* **36,** 603–622 (2004).
10. Boukharfane, R., Ribeiro, F. H. E., Bouali, Z. & Mura, A. A combined ghost-point-forcing/direct-forcing immersed boundary method (IBM) for compressible flow simulations. *Computers & Fluids* **162,** 91–112 (2018).

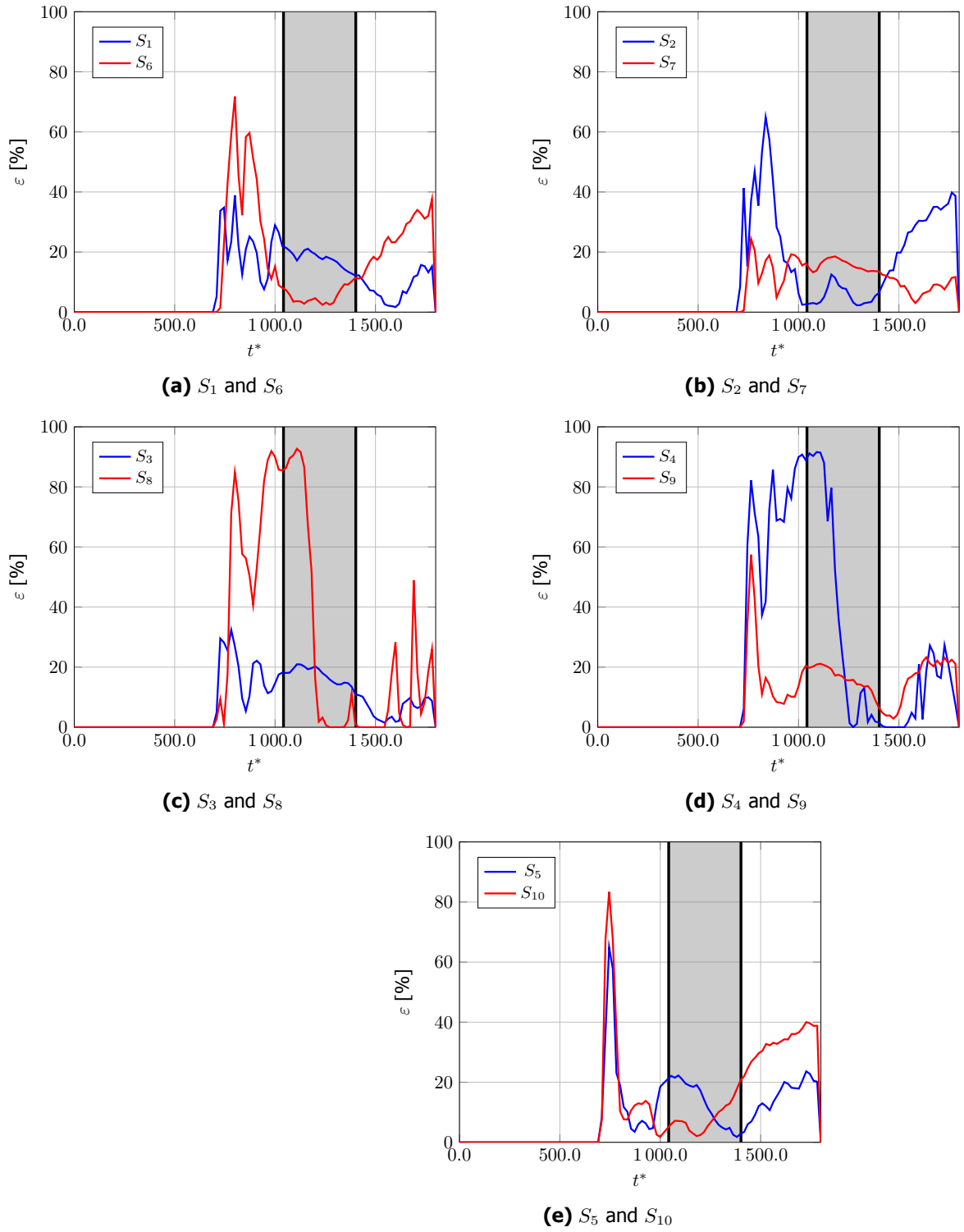

(a) S_1 and S_6

(b) S_2 and S_7

(c) S_3 and S_8

(d) S_4 and S_9

(e) S_5 and S_{10}

Fig 12. Error between the measured pressure in the experiment and the calculated one in the simulation

11. Celik, I., Cehreli, Z. & Yavuz, I. Index of resolution quality for large eddy simulations. *Journal of fluids engineering* **127,** 949–958 (2005).

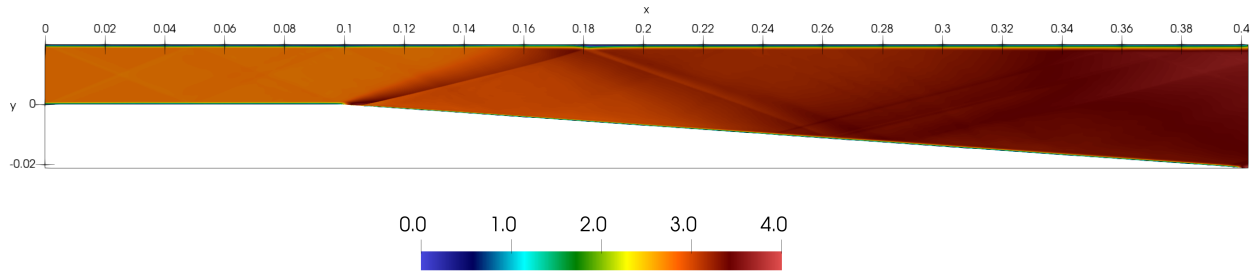

Fig 13. Mach number

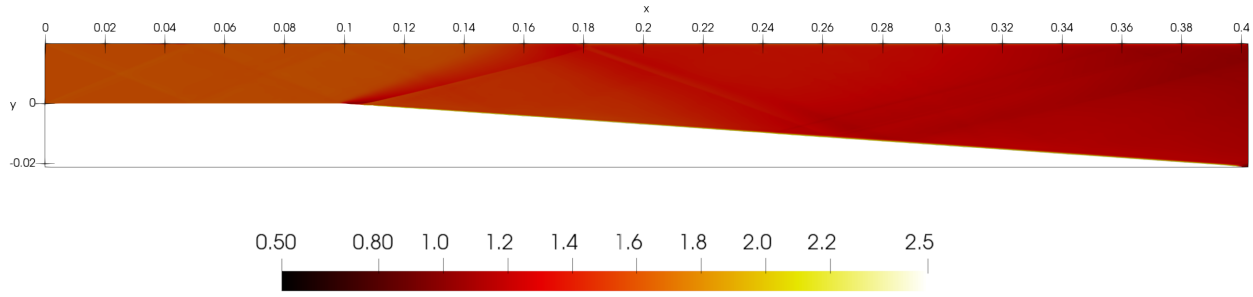

Fig 14. Normalized temperature

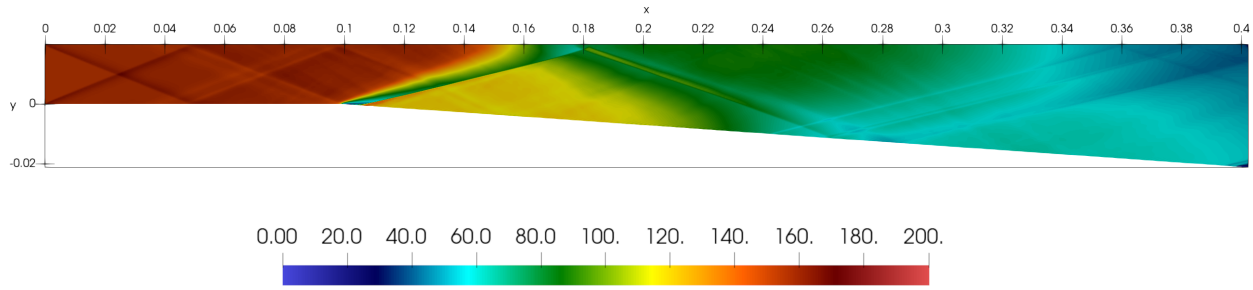

Fig 15. Normalized pressure

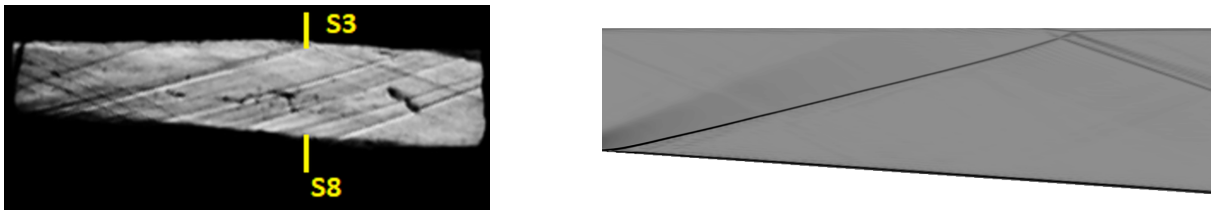

(a) Experiment **(b)** CFD

Fig 16. Schlieren comparison between experiment and CFD

12. Techer, A. *Simulation aux grandes échelles implicite et explicite de la combustion supersonique* PhD thesis (ISAE-ENSMA Ecole Nationale Supérieure de Mécanique et d'Aérotechique-Poitiers, 2017).